https://doi.org/10.5194/egusphere-2026-6619
Preprint. Discussion started: 23 November 2026
© Author(s) 2026. CC BY 4.0 License.

Contrail Tracking, Flight Matching, and Thermodynamic Analysis of Formation Conditions

Simon Kröger[1], Sebastian Lück[1], and Jan Goeing[1]

[1]Institut of Jet-Propulsion and Turbomachinery
Technische Universität Braunschweig
Hermann-Blenk-Str. 37, 38108 Braunschweig, Germany

Correspondence: Sebastian Lück (s.lueck@tu-braunschweig.de) and Jan Goeing (j.goeing@tu-braunschweig.de)

Abstract. Validation of condensation trail (contrail) prediction tools requires large datasets of real-world contrail observations clearly linked to the emitting aircraft. This link allows the time and location of contrail formation to be determined, which in turn enables the conditions at formation to be identified. Methods available in the literature for matching contrail observations with flight trajectories involve considerable uncertainty regarding matching accuracy. Hence, this paper presents an improved method for matching contrails with flight trajectories using time series of contrail observations rather than single observations alone. Contrails identified in satellite images are tracked from their first to their last observation. This is achieved by linking observations across successive time steps using a decision tree and iteratively refined estimates of contrail altitude. Matching is performed by comparing the observed contrail tracks with hypothetical contrail tracks calculated from flight trajectories and atmospheric data. In particular, knowledge of the first observation, together with the subsequent evolution of the contrail, enables more accurate matching than relying solely on a single observation. The most likely emitting flight is selected from the candidate matches. The resulting associations were used to determine the location and time of contrail formation. The method was applied to all 53 Mondays in 2024, each covering a 24-hour period, within an area of 1100 km × 1100 km. The conditions at contrail formation were analysed and assessed for consistency with the Schmidt–Appleman criterion. Although uncertainties remain, general agreement with the criterion was observed. In the long term, this approach could support linking conditions at contrail formation to aircraft performance, engine performance, and emission data, enabling multidisciplinary analysis of contrail formation.

1 Introduction

The understanding, prediction and re-analysis of aviation induced contrail cirrus is growing ever further, becoming a major focus of research in non-CO2 emissions of aviation (Lee et al., 2021; Bickel et al., 2025; Teoh et al., 2023, 2020) and their avoidance (Sausen et al., 2024; Roosenbrand et al., 2023). Microphysics of contrail formation are investigated based on detailed measurements of the engine plume, which are then used to build and improve contrail formation models. The amount of in-flight measurements is scarce, with a total of 33 studies accounted for by Schumann et al. (2017). Therefore, the validation datasets are limited to either specific aircraft types that are available at the large research facilities and used in chase plane experiments at DLR or NASA over limited geographical extent at specific atmospheric conditions during that flight (Jeßberger

https://doi.org/10.5194/egusphere-2026-6619
Preprint. Discussion started: 23 November 2026
© Author(s) 2026. CC BY 4.0 License.

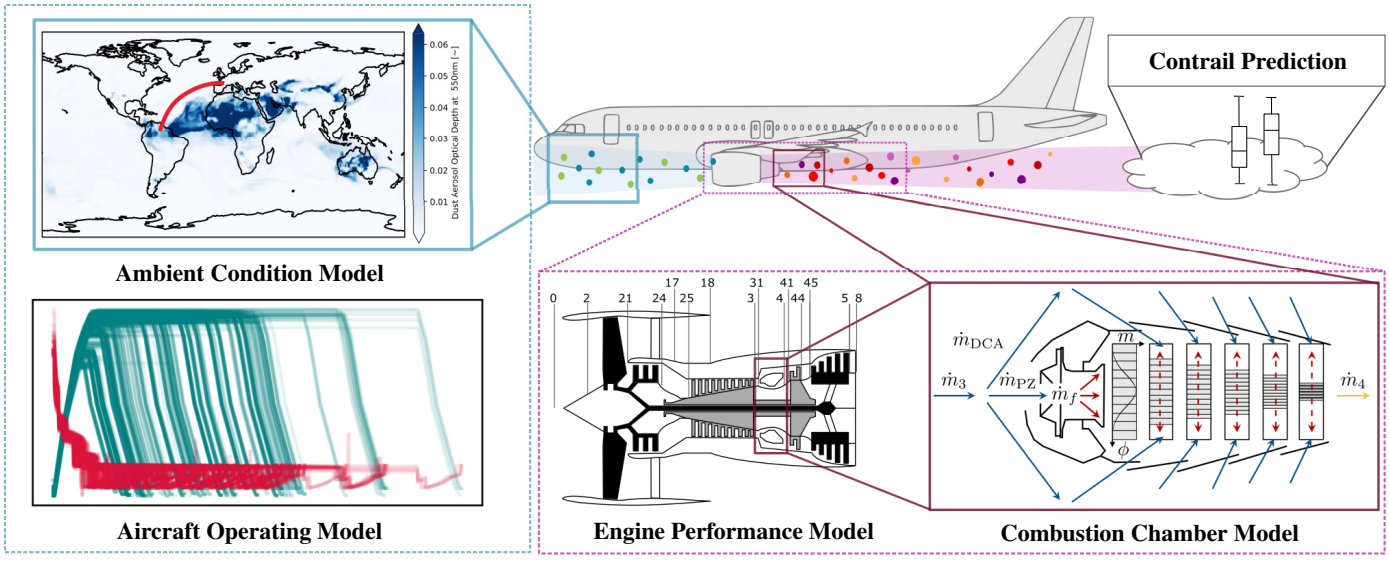

Figure 1. Platform 'Modelling and System analysis of Aero Engines' (MSAE) (Lieder et al., 2025).

et al., 2013). While these flights deliver high fidelity measurements and insights, the underlying experiments are costly and resource-consuming, clearly limiting the extent of these endeavors. Hence, there is a substantial need for alternate sources of validation data for contrail models to improve existing tools such as CoCiP (Schumann et al., 2017; Schumann, 2012) and add more validation data, especially in ice saturated regions (Schumann and Heymsfield, 2017; Kärcher, 2018).

Such validation datasets may be provided by using observational data from satellite imagery, which are then connected to airplane movements (Riggi-Carrolo et al., 2023; Chevallier et al., 2023; Sarna et al., 2025; Meijer et al., 2024; Vazquez-Navarro et al., 2010).

Beyond the aspect of linking airplane movement and contrail observation, the issue of contrail formation is not limited to the microphysics outside the aircraft engine (Schumann, 1996). On the contrary, it depends on a multitude of parameters which are the thermodynamic properties at the engine exhaust, as well as the soot particles involved. These parameters, in turn, depend on the aircraft type, flight profile (distance travelled, total distance), and the state of the aircraft (current weight, thrust, etc.), and atmospheric conditions (temperature, humidity) at the contrail origin. Therefore, an entire tool chain is required to cover the various aspects and provide a multimodal dataset which can be ingested into contrail predictions. An example was presented in Lieder et al. (2025) where an atmospheric model, an aircraft operating model, an engine performance model, and a combustor model were applied to a flight mission to provide this essential data (see fig. 1).

Commonly, contrails are identified within satellite images using an image recognition model. Subsequently, they are matched to a flight trajectory using a geometric matching algorithm. However, substantial uncertainties arise when an arbitrary image is used as a contrail observation. Wind velocity and direction can be substantially different over common aircraft flight altitudes,

https://doi.org/10.5194/egusphere-2026-6619
Preprint. Discussion started: 23 November 2026
© Author(s) 2026. CC BY 4.0 License.

hence matching a flight with a contrail observation long after its emission and formation becomes difficult. It was shown that tracking the contrail over multiple images before matching it can substantially reduce uncertainty (Chevallier et al., 2023; Kröger et al., 2025).

This paper provides a framework for automated tracking of contrails over multiple satellite images throughout their lifetime. This includes dissemination of data sources, contrail identification using publicly available AI models, tracking and clustering of contrails and contrail segments over multiple frames, and the identification of the contrail origin in space and time. The steps are described in-depth to guide through the entire matching and tracking process.

Hence, application of the framework allows the user to link an observed contrail in an arbitrary frame to a) its origin or initial observation and b) link it to an airplane movement. Its trajectory can then be used to determine the aircraft performance and engine conditions during contrail formation. This study provides an enhancement to previous studies (Kröger et al., 2025) by introducing additional evaluation metrics, automated tracking, and the capability to analyze large datasets.

We intend to contribute with this method a proof-of-concept of the tracking method to then create a large observation based dataset, that can be used to identify and track contrails, analyze their persistency, and suggest a method to enrich this dataset with a clear connection to airplane movements by including ADS-B data. Subsequently, further information, such as flight kinetics and aero engine performance simulations can be included into comprehensive analysis of large datasets that include aircraft types, thermodynamic engine performance parameters, and engine emissions (particulate emissions, particle sizes etc.). With such a dataset, future conclusions may be drawn on contrail formation using all information on the specific topics mentioned before.

2 Methods

Figure 2 illustrates the basic workflow of the method. Each solid box represents a processing step, whereas the dotted boxes represent a specific state of the data. Each processing step is described in a corresponding section of this chapter. The initial data sources are presented in Section 2.1.

In the first processing step (I), contrails are detected using an implementation of a contrail detection algorithm. The algorithm returns a binary pixel mask indicating whether each pixel belongs to a contrail. Because this representation is not suitable for tracking and matching, a line-segmentation algorithm was developed to extract individual contrail lines from these masks (II). The extracted lines are then grouped in space and time so that the evolution of an individual contrail can be tracked over time (III).

The grouped line segments are subsequently matched with air traffic data using the matching algorithm (IV), resulting in an association between contrails and individual flights. In the fifth step (V), the section of the flight trajectory in which the contrail has formed is identified, and the corresponding atmospheric conditions at the formation location are determined.

https://doi.org/10.5194/egusphere-2026-6619
Preprint. Discussion started: 23 November 2026
© Author(s) 2026. CC BY 4.0 License.

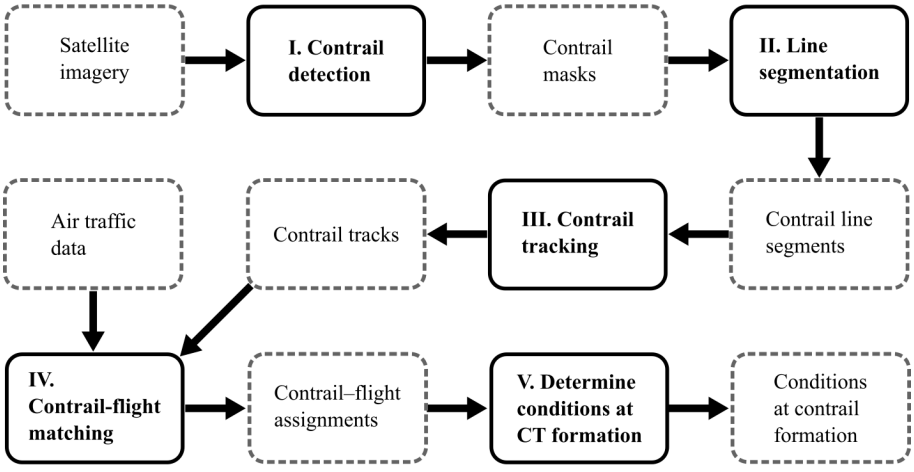

Figure 2. Workflow of the presented method. Solid boxes represent processing steps, whereas dotted boxes represent intermediate data states. Each processing step corresponds to a section in this chapter.

2.1 Data

This method requires three datasets. The first consists of satellite imagery used for contrail detection. The second comprises air traffic data used to match detected contrails with individual flights. The third consists of atmospheric data, including wind vectors for contrail matching and tracking, as well as variables such as temperature and humidity for determining the atmospheric conditions at the time of contrail formation.

2.1.1 Satellite imagery

For the satellite imagery, geostationary GOES-East Continental United States (CONUS) data provided by the National Oceanic and Atmospheric Administration (NOAA) were used. The imagery has a temporal resolution of five minutes and a spatial resolution of approximately $2\,\mathrm{km} \times 2\,\mathrm{km}$. It comprises 16 spectral channels ranging from the visible to the infrared spectrum.

The images are transformed into the ash color scheme, a three-channel representation composed of different infrared bands. This representation improves contrail visibility and enables consistent detection during both daytime and nighttime (Ng et al., 2024). Subsequently, $(1100\,\mathrm{km} \times 1100\,\mathrm{km})$ image patches are generated by reprojecting the data onto a Lambert Conformal Conic (LCC) projection. The latitude and longitude of origin are set to the center of each patch, while the two standard parallels are positioned approximately one-sixth of the patch height from the upper and lower boundaries, respectively. Finally, the reprojected data are resampled onto a regular grid of (512×512) pixels.

The main advantages of using these images are their extensive spatial coverage, high temporal resolution, easy accessibility, and the fact that the OpenContrails dataset (Ng et al., 2023), which was used to train the contrail detection algorithm, is based on the same type of satellite imagery.

https://doi.org/10.5194/egusphere-2026-6619
Preprint. Discussion started: 23 November 2026
© Author(s) 2026. CC BY 4.0 License.

The main disadvantage of geostationary satellite imagery is its comparatively low spatial resolution due to its distance from the earth, which limits the detection of newly formed and optically thin contrails. Consequently, a time delay is expected between contrail formation and its first observation in the satellite imagery. This also suggests that the detected contrails are predominantly persistent contrails.

2.1.2 Air traffic data

For the air traffic data, ADS-B records from the OpenSky Trino Historical Database were used. OpenSky collects data from commercially available ADS-B sensors operated by volunteers worldwide (Schafer et al., 2014). The quality and coverage of the data depend strongly on sensor density, which is particularly high in Europe and North America (Sun et al., 2024). Based on the findings and filtering methods presented by Olive et al. (Olive, 2019; Olive et al., 2025), the air traffic data were preprocessed to remove erroneous and inconsistent records before being used for contrail–flight matching.

2.1.3 Atmospheric data

For the atmospheric data, the ERA5 reanalysis dataset provided by the European Centre for Medium-Range Weather Forecasts (ECMWF) was used (Hersbach et al., 2020). The dataset has a temporal resolution of one hour, a horizontal spatial resolution of approximately $(31\,\mathrm{km} \times 31\,\mathrm{km})$, and global coverage. To obtain a higher vertical resolution, ERA5 model-level data were used. These data are available on 137 model levels and were interpolated onto pressure levels with a spacing of $20\,\mathrm{hPa}$.

2.2 I. Contrail Detection

For contrail detection, the winning entry of the Google AI Kaggle competition "Google Research—Identify Contrails to Reduce Global Warming," developed by Jun Kode, was used (Kode, 2023). The model achieved a global Dice coefficient of 0.724. It combines a single-frame model with a four-frame model and therefore considers not only the current image but also the three preceding images. The output is a binary pixel mask indicating which pixels are classified as part of a contrail.

The model requires input images with a resolution of (256×256) pixels. Therefore, each projected (512×512)-pixel image described in Section 2.1.1 is divided into four (256×256)-pixel tiles. Contrail detection is performed separately on each tile, after which the resulting masks are merged to reconstruct the full (512×512)-pixel detection mask. Figure 3 shows an example satellite image with the corresponding detection mask overlaid.

https://doi.org/10.5194/egusphere-2026-6619
Preprint. Discussion started: 23 November 2026
© Author(s) 2026. CC BY 4.0 License.

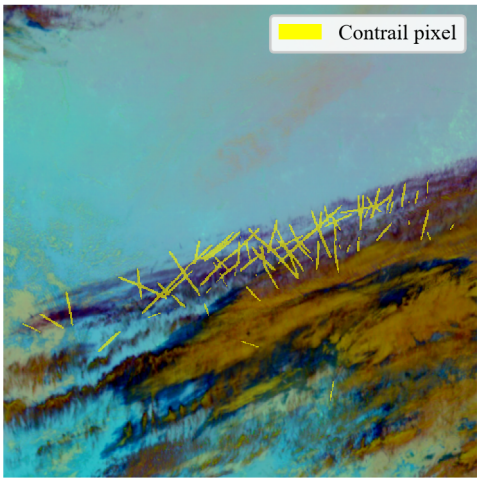

Figure 3. Example of a (512×512)-pixel satellite image cutout in Lambert conformal conic (LCC) projection using the ash color scheme, with an overlaid contrail mask.

2.3 II. Line segmentation

While the contrail detection algorithm identifies pixels that belong to contrails, it does not distinguish between individual contrails. In particular, contrails may overlap or intersect, such that a connected pixel structure does not necessarily represent a single contrail (see Figure 3).

The tracking algorithm aims to identify the predecessor of an individual contrail, while the matching algorithm links individual contrails to specific flights. It is therefore essential to separate the contrails contained in the contrail mask generated by the contrail detection algorithm. In this work, the task of extracting individual contrail line segments from the detection mask is referred to as *line segmentation*.

Several off-the-shelf methods were evaluated, including the probabilistic Hough transform (Matas et al., 2000) and the OpenCV Line Segment Detector (Debnath, 2020). However, neither approach produced satisfactory results. They struggled particularly with overlapping contrails and frequently detected multiple line segments for a single contrail. Therefore, a custom method was developed to address these limitations.

The proposed method consists of the following three steps:

1. **Skeleton-network extraction**

   The `sknw` skeleton-network algorithm (Xiaolong, 2021) is applied to the binary contrail mask. The algorithm transforms the binary mask into a network graph consisting of nodes and edges.

2. **Identification of approximately straight sections**

https://doi.org/10.5194/egusphere-2026-6619
Preprint. Discussion started: 23 November 2026
© Author(s) 2026. CC BY 4.0 License.

Within each isolated network component, a candidate connection is evaluated for every pair of nodes. The path between the respective nodes is approximated using a least-squares line, and the mean perpendicular deviation of the path points from this line is calculated. If the mean deviation is below a predefined threshold, the path is considered approximately straight and retained as a candidate line segment.

3. **Removal of redundant line segments**

   Redundant line segments are removed, particularly segments that are fully contained within longer segments. The result of the line-segmentation algorithm is shown in Figure 4.

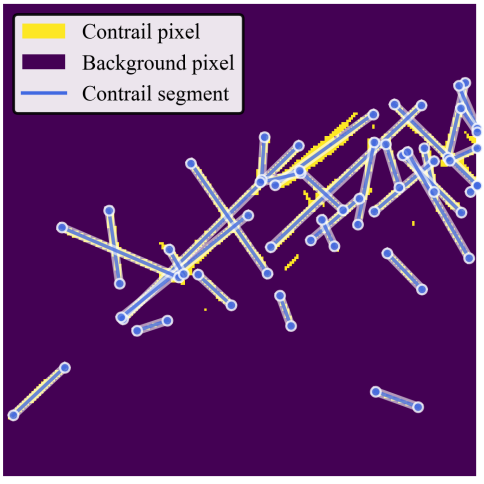

Figure 4. Example of the proposed line-segmentation algorithm applied to a binary contrail mask.

2.4 III. Contrail tracking

Contrail tracking fundamentally consists of grouping the line segments extracted in Section 2.3 across multiple time steps. The task can therefore be formulated as identifying the predecessor and successor of each contrail segment.

The main challenge is that the altitude of a contrail is generally unknown. Consequently, the atmospheric wind field cannot be used to predict its position at the subsequent time step with high precision. Owing to the five-minute temporal resolution of the GOES satellite imagery, this uncertainty is usually manageable when no other contrail segments are located nearby. However, as shown in Figure 3, contrails frequently occur in clusters, resulting in several competing successor candidates.

To improve the prediction and distinguish between these candidates, a probabilistic approach based on Bayesian principles is introduced. Predictions are generated for different contrail altitudes and assigned corresponding probabilities. These probabilities are updated after each tracking step based on the previously established connections. In this way, the most likely altitude can gradually be estimated, improving subsequent position predictions and the selection of suitable successor segments.

The proposed tracking method consists of four main steps:

https://doi.org/10.5194/egusphere-2026-6619
Preprint. Discussion started: 23 November 2026
© Author(s) 2026. CC BY 4.0 License.

1. **Prefiltering of potential successors**

   For each line segment, a successor search region is generated for the subsequent time step. Figure 5 illustrates how this region is constructed.

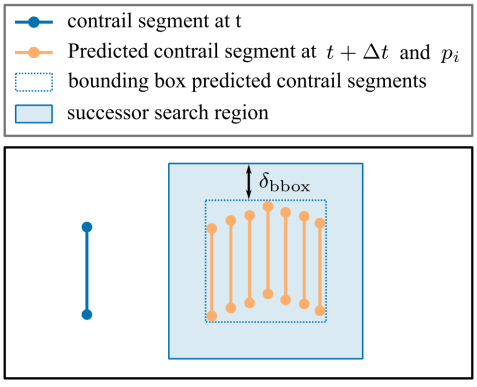

Figure 5. Schematic representation of the construction of the successor search region at $t + \Delta t$ for a single contrail segment at t. In this example, the general wind direction is from west to east; therefore, the successor search region is located east of the contrail segment.

The predicted segment position is calculated for all considered pressure levels p_i, corresponding in this case to intervals of $20\,\mathrm{hPa}$ above an altitude of approximately $6\,\mathrm{km}$. For each pressure level, the segment is advected using the corresponding atmospheric wind field to estimate its position at the next time step.

The successor search region is then defined as a rectangular bounding box enclosing all predicted segment positions. An additional margin δ_{bbox} is applied to account for uncertainties in the wind data and the resulting position estimates.

All line segments at the subsequent time step that intersect or lie within the successor search region are retained as potential successors. Figure 6a shows the contrail segments at times (t) and $(t + \Delta t)$, together with the corresponding successor search regions.

Figure 6b shows the resulting network graph. In this representation, contrail segments are represented by nodes, while possible connections are represented by edges. Some assignments are unambiguous, as illustrated by the connection between (N4) and (N8). However, a segment may have multiple possible predecessors, as in the case of (N5) and (N6) for (N1), or multiple segments may compete for the same successor, as shown by (N2) and (N3) competing for (N7).

Therefore, in the next step, each edge is assigned a score representing the plausibility of the corresponding connection. These scores are subsequently used to determine the most likely predecessor-successor assignments.

2. **Scoring of candidate connections**

To resolve the ambiguous connections between the contrail segments shown in Figure 6, a connection score s_{con} is introduced. This score quantifies the plausibility of each connection and is defined as

https://doi.org/10.5194/egusphere-2026-6619
Preprint. Discussion started: 23 November 2026
© Author(s) 2026. CC BY 4.0 License.

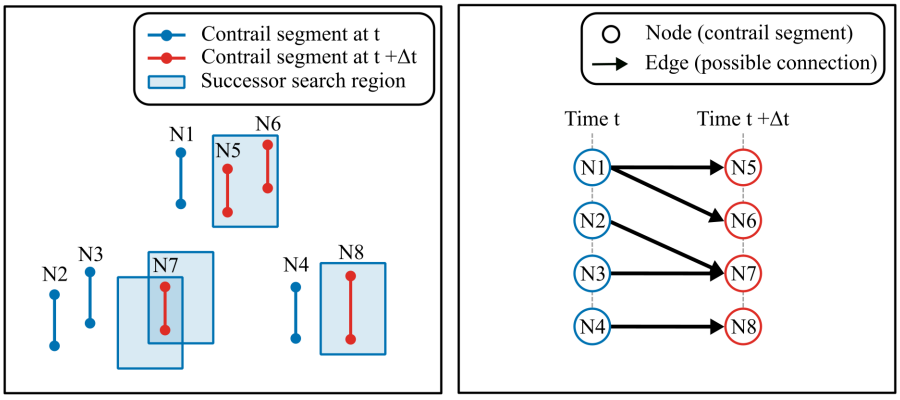

(a) contrail segments in image space (b) resulting graph representation

Figure 6. In (a), contrail segments at two consecutive time steps, (t) and $(t + \Delta t)$, are shown together with the successor search regions of the segments at time (t). In (b), the same two time steps are represented as a graph used to resolve competing successor and predecessor assignments.

$$s_{\mathrm{con}} = \sum_{i=1}^{n} q_i \, s_{\mathrm{t},i} \qquad \text{with} \qquad \sum_{i=1}^{n} q_i = 1. \tag{1}$$

Here, $s_{\mathrm{t},i}$ denotes the agreement between the observed successor segment and the predicted segment position at pressure level i. These predicted positions are the same as those used to construct the successor search region shown in orange in Figure 5. The value q_i represents the estimated probability that the contrail is located at pressure level i.

All pressure levels are initially assigned equal probabilities:

$$q_{i,\mathrm{init}} = \frac{1}{n}, \tag{2}$$

where n denotes the number of pressure levels considered. After each successful tracking step, the corresponding probabilities are updated according to

$$q_{i,t+1} = \frac{q_{i,t} \cdot s_{\mathrm{t},i}}{\sum_j q_{j,t} \cdot s_{\mathrm{t},j}}. \tag{3}$$

Consequently, the algorithm assigns greater weight to pressure levels whose predictions have agreed well with observations during previous tracking steps. In this way, information gained from earlier tracking steps improves the resolution of ambiguous connections in the decision tree such as those shown in Figure 6.

https://doi.org/10.5194/egusphere-2026-6619
Preprint. Discussion started: 23 November 2026
© Author(s) 2026. CC BY 4.0 License.

The agreement score $s_{\mathrm{t},i}$ is calculated from three individual criteria: the distance score s_{d}, the angular-alignment score s_{a}, and the overlap score s_{o}. These scores are combined using a weighted geometric mean, with the weights w shown in Table 1:

$$s_{\mathrm{t},i} = s_{\mathrm{d},i}^{w_{\mathrm{d}}} \cdot s_{\mathrm{a},i}^{w_{\mathrm{a}}} \cdot s_{\mathrm{o},i}^{w_{\mathrm{o}}}. \tag{4}$$

Table 1. Standard deviations and weights used for the individual connection-scoring criteria.

Criterion	**Standard deviation σ**	**Weight w**
Distance d	10 km	0.7
Angular difference a	5°	0.2
Overlap $o1$	20 %	0.1

Each individual score is calculated using a Gaussian function:

$$s_k = \exp\left(-\frac{x_k^2}{2\sigma_k^2}\right), \qquad k \in \mathrm{d}, \mathrm{a}, \mathrm{o}, \tag{5}$$

where x_k denotes the corresponding deviation measure and σ_k controls the sensitivity of the score. The standard deviations used for the three criteria are listed in Table 1. The deviation values x_k are illustrated in Figure 7 and defined by Equations 6, 7, and 8.

$$x_d = \frac{l_1 + l_2}{2} \text{ in km} \tag{6}$$

$$x_a = \alpha \text{ in } ^\circ \tag{7}$$

$$x_{o1} = \frac{\frac{l_4}{l_3} + \frac{l_6}{l_5}}{2} \text{ in 1} \tag{8}$$

3. Selection of Connections

After all feasible connections between contrail segments have been identified and their quality has been evaluated using the connection score s_{con}, the most likely connections are selected to obtain a unique assignment between segments at

https://doi.org/10.5194/egusphere-2026-6619
Preprint. Discussion started: 23 November 2026
© Author(s) 2026. CC BY 4.0 License.

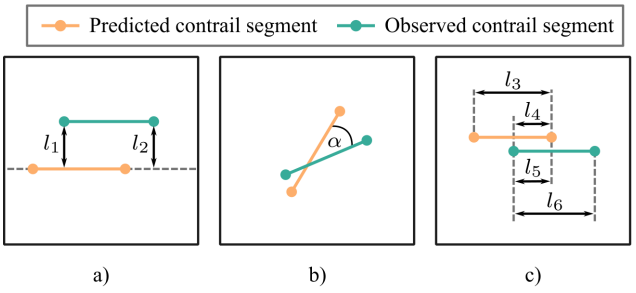

Figure 7. Illustration of how the x_k values are calculated. Panel (a) shows the distance deviation x_d defined in Equation 6, panel (b) shows the angular deviation x_a defined in Equation 7, and panel (c) shows the overlap deviation x_o defined in Equation 8.

two consecutive time steps. Since multiple segments may compete for the same successor, the assignment cannot be determined independently for each segment but must be solved globally.

The problem is therefore formulated as a weighted bipartite assignment problem and solved using the Kuhn–Munkres algorithm (Hungarian method) (Kuhn, 2010; Crouse, 2016). For each pair of consecutive time steps, the connection scores are arranged in a matrix, which is multiplied by -1 to convert the maximization of connection scores into the minimization problem required by the algorithm. Connections with $s_{\mathrm{con}} < 0.1$ are treated as invalid and discarded.

The resulting assignment provides a unique mapping between contrail segments of two consecutive time steps. Based on this mapping, the probabilities can be updated according to Eq. 3 and propagated to the next time step. By applying this procedure sequentially from the first to the final time step, temporally connected groups of contrail segments are obtained.

4. **Grouping of collinear segment tracks**

The assumption that each contrail segment can have only a single successor introduces a limitation, since real contrails may split into multiple subsequent structures.

To account for this, fragmented contrails are merged into a common contrail if the segments are mutually collinear at all time steps in which both sequences are present. Here, collinearity refers to a similar segment orientation and a spatial arrangement consistent with a common line extension.

A difficulty arises when pairwise collinearity does not hold across an entire group of segments. Figure 8 illustrates this case using three segments: A and B satisfy the collinearity criterion, as do B and C, whereas A and C do not. It must therefore be decided which associations to retain. This ambiguity can also occur in more complex configurations involving multiple competing segment tracks.

To resolve these ambiguities, a collinearity score is computed between candidate segment tracks, analogous to the scoring approach introduced in Step 2. Starting with the highest-scoring association, additional segment tracks are added to a group only if they are collinear with all tracks already contained in that group. This procedure is repeated until no further

https://doi.org/10.5194/egusphere-2026-6619
Preprint. Discussion started: 23 November 2026
© Author(s) 2026. CC BY 4.0 License.

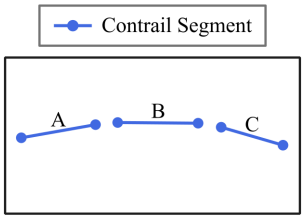

Figure 8. Ambiguous associations between three segments. Segment B satisfies the collinearity criterion with both A and C, while A and C do not satisfy it with each other.

compatible group member can be identified. In this way, each resulting group consists exclusively of mutually collinear segment tracks and can subsequently be treated as one common contrail.

2.5 IV. Contrail-flight matching

After the contrail segments generated by the line-segmentation procedure (II) have been linked into contrail tracks (III), the next step is to associate these tracks with potential source flights.

The main challenge is the unavoidable time gap between contrail formation and its first detection in satellite imagery. Newly formed contrails are often too narrow to be detected immediately due to the spatial resolution of the geostationary satellite imagery (approximately 2 km per pixel) and the discrete temporal sampling interval of 5 min. Consequently, contrails observed in the satellite images are generally displaced from their formation locations due to advection by the ambient wind.

This temporal and spatial gap can be bridged in two directions: either by propagating the observed contrail backward toward a potential source flight or by propagating individual flights forward to predict the location of a potentially generated contrail. Both approaches have specific disadvantages. Backward propagation of the contrail is inherently uncertain because its formation altitude is initially unknown, whereas forward propagation of all available flights is computationally expensive.

Therefore, a hybrid approach is used that combines both strategies. First, computationally cheap backward propagation from the observed contrail is used to identify a small number of plausible source-flight candidates. For these candidates, the more precise but costly forward propagation is then applied to further narrow down the set of possible source flights, identify the best-matching candidate, and determine the likely time and location of contrail formation. The procedure consists of the following steps:

1. **Preselection of candidate flights**

   To identify an initial set of candidate source flights, the endpoints of the contrail track at the first observation time are advected backward in time using the wind field. Since the contrail altitude is unknown, this procedure is performed at all considered pressure levels, spaced at intervals of $20\,\mathrm{hPa}$ within an altitude range of 6–$15\,\mathrm{km}$. The contrail is assumed to remain at a constant altitude.

https://doi.org/10.5194/egusphere-2026-6619
Preprint. Discussion started: 23 November 2026
© Author(s) 2026. CC BY 4.0 License.

A bounding prefilter rectangle enclosing all these trajectories is then constructed and expanded to account for potential uncertainties. An example is shown in figure 9a, highlighting the advection vectors of the endpoints (orange). Flights are selected if their trajectories intersect this prefilter rectangle (green) during the interval from $t_0 - 70\,\mathrm{min}$ to t_0, where t_0 denotes the first observation.

Additionally, the orientation of each flight trajectory within the prefilter rectangle must differ by no more than $30°$ from the contrail orientation at the first observation. Figure 9b shows examples of flights satisfying both criteria (red). The flight trajectory orientation is determined by fitting a line through all trajectory points within the prefilter rectangle using least squares.

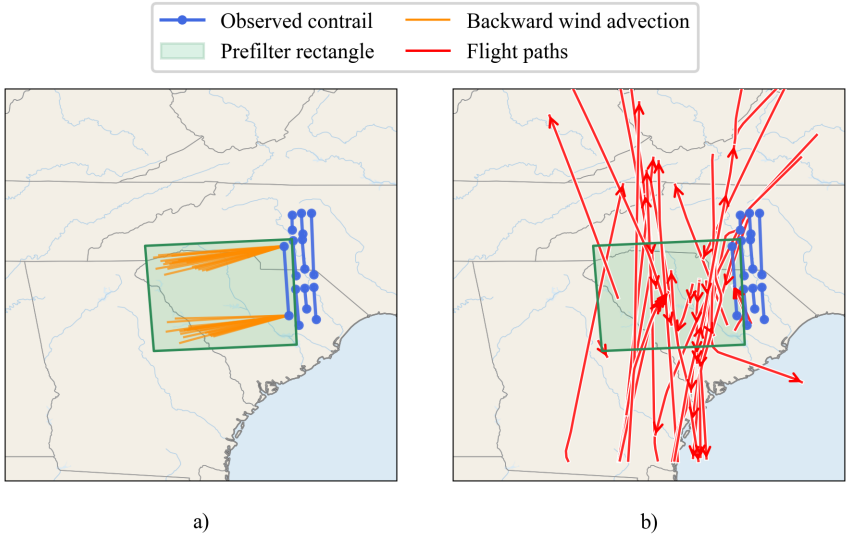

Figure 9. Example of the prefiltering process. Panel (a) illustrates the construction of the prefilter rectangle, while panel (b) shows the flights satisfying the prefiltering criteria.

2. **Calculation and filtering of hypothetical contrail trajectories**

In the next step, hypothetical contrails are computed for the flights selected during prefiltering in the previous step (Figure 10a). These represent the expected contrail positions, assuming that the flights produced contrails. They are obtained by advecting individual points along each flight trajectory forward in time using the wind field.

The hypothetical contrails are then assessed for spatial agreement with the observed contrail (blue). A rectangle with an initial width of $28\,\mathrm{km}$ is constructed around and aligned with the observed contrail (green), and only hypothetical contrails intersecting this rectangle are retained (solid, colored). Additionally, their orientation must differ by no more than $14°$ from that of the observed contrail. The orientation is determined using the same approach as in prefiltering, by fitting a line to all hypothetical contrail points within the postfilter rectangle using least squares. Figure 10a shows the

https://doi.org/10.5194/egusphere-2026-6619
Preprint. Discussion started: 23 November 2026
© Author(s) 2026. CC BY 4.0 License.

hypothetical contrails corresponding to the flights (dashed) in Figure 9b, with those satisfying both criteria highlighted in color.

This comparison is repeated at all subsequent contrail observations. To account for the increasing uncertainty in the calculated positions over time, the rectangle is expanded by $1\,\mathrm{km}$ and the angular tolerance is increased by 1° at each successive observation. This prevents the filtering criteria from becoming overly restrictive for contrails tracked over many time steps. Figure 10b compares the observed and calculated contrail positions across multiple time steps for the three flights that satisfy these criteria. It is visible, that the hypothetical contrails agree to a different extent and further assessment is required in the next step.

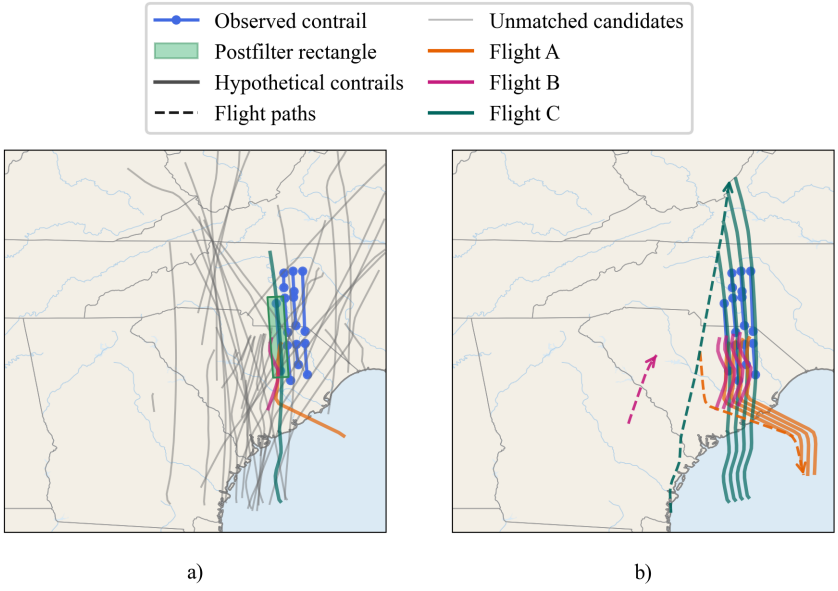

Figure 10. Example of the comparison between hypothetical and observed contrails. Panel (a) illustrates the initial filtering step, in which all potential contrails are compared with the first observed contrail using a surrounding rectangle and an orientation criterion. Panel (b) compares the observed contrail with the hypothetical contrails associated with three flights that satisfy the filtering criteria across multiple observation times.

3. Quantification of agreement between observed and hypothetical contrails

As illustrated in Figure 10b, the agreement between observed and predicted contrail positions can vary even when the filtering criteria are satisfied. This agreement is therefore quantified using a matching quality score. The approach follows the line comparison method used in step 2 of the tracking procedure described in Section 2.4.

For each observation time i, an individual score $s_{\mathrm{qual},i}$ is calculated according to Equation 4 as a weighted combination of subscores representing distance, angular difference, and overlap. The initial standard deviations and weights used for matching are listed in Table 2.

https://doi.org/10.5194/egusphere-2026-6619
Preprint. Discussion started: 23 November 2026
© Author(s) 2026. CC BY 4.0 License.

Table 2. Initial standard deviations and weights used for the individual matching criteria.

Criterion	Initial standard deviation σ	Weight w
Distance d	$7\,\mathrm{km}$	0.5
Angular difference a	7.5°	0.3
Overlap $o2$	$20\,\%$	0.2

For matching, the overlap score s_{o2} is defined using the lengths l_6 and l_7 illustrated in Figure 11:

$$s_{o2} = \frac{l_7}{l_6}. \tag{9}$$

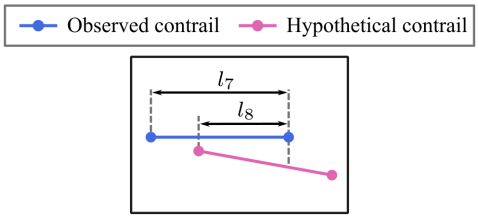

Figure 11. Geometric definition of the lengths l_6 and l_7 used to calculate the overlap score s_{o2} for source flight matching according to Equation 9.

To account for increasing prediction uncertainty over time, the standard deviations for the distance and angular difference subscores are gradually increased from their initial values by $1\,\mathrm{km}$ and 1° per observation step, respectively. The overlap standard deviation and the criterion weights remain constant.

The individual scores are then combined into an overall matching quality score $s_{\mathrm{qual,total}}$ using an exponentially weighted average:

$$s_{\mathrm{qual,total}} = \frac{\sum_{i=0}^{n-1} \lambda^i s_{\mathrm{qual},i}}{\sum_{i=0}^{n-1} \lambda^i}, \qquad 0 < \lambda < 1, \tag{10}$$

where n is the number of observation times, $i = 0$ denotes the first observation, and $\lambda = 0.75$ controls the decrease in weight for successive observations. Earlier observations receive greater weight because the elapsed time between contrail formation and observation is shorter, and the associated advection errors are therefore assumed to be smaller.

In the example shown in Figure 10b, Flight C achieves an overall matching quality score $s_{\mathrm{qual,total}}$ of 0.95, while Flights B and A achieve scores of 0.10 and 0.21, respectively.

4. Quantification of the uniqueness of the contrail–flight assignment

https://doi.org/10.5194/egusphere-2026-6619
Preprint. Discussion started: 23 November 2026
© Author(s) 2026. CC BY 4.0 License.

Subsequently, a confidence score is calculated to indicate whether there are other (less plausible) matching flights for the given contrail. It relates the quality score of one flight to those of all other hypothetical contrail sources identified.

$$s_{conf} = \frac{s_{\mathrm{qual,i}}}{\sum_j s_{\mathrm{qual,j}}}. \tag{11}$$

The confidence score assesses the best match relative to the other relevant candidates and is calculated only for the flight with the highest overall matching quality score. In the example shown in Figure 10b, Flight C has the highest score, yielding a confidence score of $0.95/(0.95+0.10+0.21) \approx 0.75$. This indicates that alternative candidates exist, but their combined matching quality is substantially lower than that of Flight C.

5. **Determination of the contrail formation location and time** Finally, the contrail with the highest quality score is used to determine the origin of the contrail on the flight trajectory as shown in fig. 12. Since the hypothetical contrails (green) are based on the trajectory points plus wind advection, the intersection with the contrail observation (blue) can be calculated and linked to the point of origin (orange points). The final atmospheric conditions are then evaluated at these points.

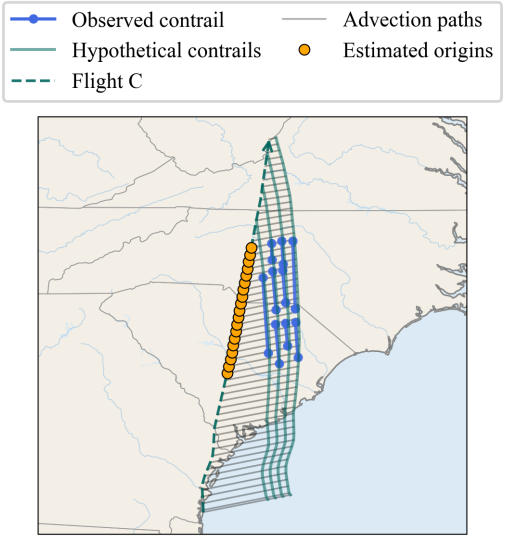

Figure 12. Illustration of how the origin of a contrail is determined. Hypothetical contrails are calculated by wind advection of points sampled along the flight trajectory. Points near the observed contrail are then traced back to their original positions to determine the time and location of contrail formation.

https://doi.org/10.5194/egusphere-2026-6619
Preprint. Discussion started: 23 November 2026
© Author(s) 2026. CC BY 4.0 License.

3 Results

This chapter evaluates the behavior and performance of the proposed method. First, the underlying dataset is introduced. Tracking and matching performance are then evaluated using selected metrics. Finally, environmental conditions at the identified contrail formation locations are compared with those of the remaining flight data to assess systematic differences.

3.1 Dataset

The method described in section 2 is applied to the geographic area shown in fig. 13. This region was chosen because of its good ADS-B data coverage. Contrail detection is performed within the satellite image area (blue). Air traffic data are collected over a larger region (orange), extending 300 km beyond the satellite image area, while atmospheric data are downloaded for an even larger region (purple), extending an additional 400 km beyond the air traffic data domain. These buffers are used because flights responsible for contrails observed within the satellite image area may have generated those contrails outside that area. Since calculating hypothetical contrails requires atmospheric data, the atmospheric data domain is chosen to be sufficiently large to support these calculations for all flights within the air traffic data domain.

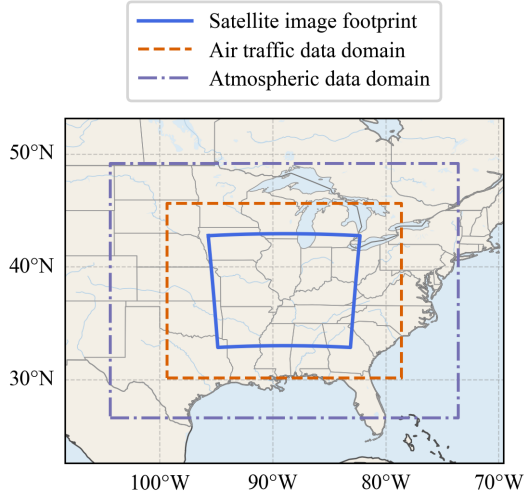

Figure 13. Geographic coverage of the datasets used in the presented statistical analysis.

The analysis covers 53 24-hour periods corresponding to all Mondays in 2024. Air traffic and atmospheric datasets are complete for these periods, whereas satellite images are missing on several occasions.

A total of 36,408 contrails were detected. As explained in section 2.4, each detected contrail represents a group of contrail segments associated within and across time steps. Approximately 21% of these contrails were classified as invalid because they were first detected in an initial satellite image of a time period, immediately after a missing satellite image, or within 30 km of

https://doi.org/10.5194/egusphere-2026-6619
Preprint. Discussion started: 23 November 2026
© Author(s) 2026. CC BY 4.0 License.

the satellite image footprint boundary. These contrails are assumed to be only partially observed and were therefore excluded, leaving 28,747 contrails for the analysis.

Approximately 1.27 million flights above altitudes of 6 km within the selected time periods and geographic domain were included in the dataset and considered for matching with the detected contrails. This altitude threshold reflects the assumption that contrails do not form below 6 km.

The processed data volumes are summarized in table 3, while the execution times for data downloads and processing steps are reported in table 4. Downloading and processing one day of data takes approximately three hours on consumer-grade hardware, resulting in a total runtime of approximately six to seven days for the entire dataset when processed sequentially. These times exclude contrail detection, which requires GPU acceleration to achieve practical runtimes and was therefore performed separately.

Table 3. Processed data sizes after spatial cropping of satellite images and resampling of traffic data to 10-second intervals. All values are in GB.

Data type	Daily average	Entire dataset (53 days)
Traffic data	0.263	13.935
Atmosphere data	0.115	6.092
Satellite images	1.207	63.983
Total	1.585	84.010

Table 4. Execution times for data downloads and processing steps on consumer-grade hardware. All values are in minutes. Contrail detection is excluded, as it was performed on a separate GPU to avoid excessive runtime.

Step	Daily average	Entire dataset (53 days)
Satellite image download	19.3	1020.8
Traffic data download	26.4	1399.20
Atmosphere data download	81.3	4310.5
Traffic processing	23.7	1254.0
Contrail segmentation	0.6	29.9
Contrail tracking	1.8	96.7
Contrail matching	18.5	978.8
Total	171.6	9089.9

3.2 Contrail Tracking Characteristics and Matching Performance

Contrails are tracked for an average of 4.87 time steps, corresponding to approximately 20 to 25 minutes. However, around 35% are detected at only a single time step, while more than 10% are tracked for over an hour. The mean contrail formation

https://doi.org/10.5194/egusphere-2026-6619
Preprint. Discussion started: 23 November 2026
© Author(s) 2026. CC BY 4.0 License.

duration is approximately 7 minutes. Contrail detections are more frequent between 08:00 and 14:00 local time and less frequent between 00:00 and 08:00. More contrails are detected in winter than in summer.

For approximately 18% of the contrails considered in this analysis, no matching flight is identified. Among contrails matched to a flight, the mean confidence score is 0.58, and the mean match quality score is 0.76.

3.3 Environmental Conditions at Contrail Formation

As explained in Section 2.5, the environmental conditions at contrail formation are identified for each contrail–flight match. In this section, these conditions are analyzed by comparing them with the environmental conditions included in the full flight ADS-B dataset to reveal systematic differences. In particular, their consistency with the Schmidt–Appleman criterion is assessed. This provides an indication of whether the identified contrail–flight matches are plausible overall.

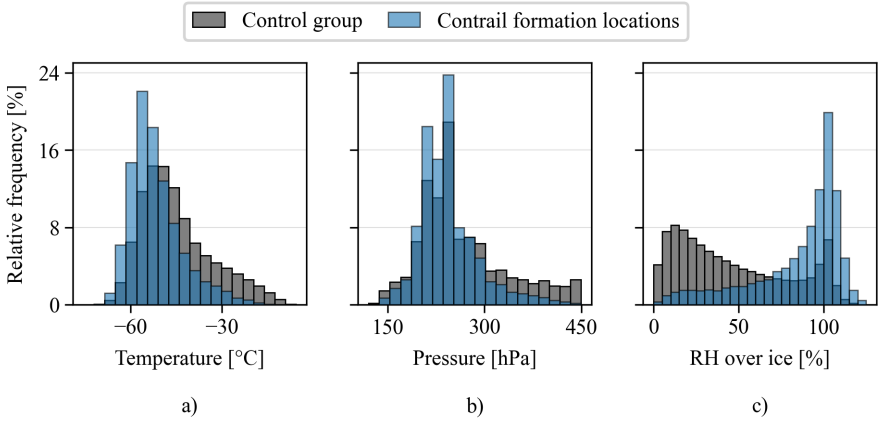

Figure 14. Relative frequency distributions of pressure, temperature, and relative humidity with respect to ice at inferred contrail formation locations and across the reference flight population.

Figure 14 shows the relative frequency distributions of the individual variables temperature, pressure, and relative humidity with respect to ice, together with the corresponding distributions of a control group. The control group consists of the environmental conditions associated with all flights within the geographic domain shown in Figure 13 during the considered time periods, restricted to altitudes above 6 km. It therefore represents all flights that could, in principle, have been matched to a contrail.

The contrail formation conditions, in contrast, are the environmental conditions along the trajectories of all valid contrail–flight matches at the locations where the flights are assumed to have produced a contrail, as shown in Figure 12. They therefore represent a small subset of the full flight dataset.

The contrail formation conditions show a higher relative frequency at higher humidity, lower temperatures, and slightly lower pressures, although the relative frequency decreases again at very low pressures. This is generally consistent with the

https://doi.org/10.5194/egusphere-2026-6619
Preprint. Discussion started: 23 November 2026
© Author(s) 2026. CC BY 4.0 License.

Schmidt–Appleman criterion, as contrail formation is favoured by lower temperatures and higher relative humidity. At higher altitudes and correspondingly lower pressures, the atmosphere also generally becomes too dry for contrail formation.

However, a substantial proportion of the identified contrail formation conditions have a relative humidity with respect to ice below 100%, which would not be expected for persistent contrails. In addition, some data points occur at temperatures above -30 °C, which are generally considered too warm for contrail formation.

When interpreting these differences, it is important to consider that the variables are not independent but are correlated through the vertical structure of the atmosphere. For example, the tendency towards lower pressures may result from the lower temperatures that typically occur at higher altitudes.

Figure 15 shows the same data as Figure 14, but in a two-dimensional representation. In this case, humidity is expressed as water vapour pressure rather than relative humidity. The control group is shown on the right, while the contrail formation conditions are shown on the left. Each area represents the relative frequency of data points within that region. The saturation lines for water and ice are also shown, together with the corresponding supersaturation regions.

The contrail formation data are clearly more concentrated near the ice saturation line, particularly at temperatures between -60 and -50 °C.

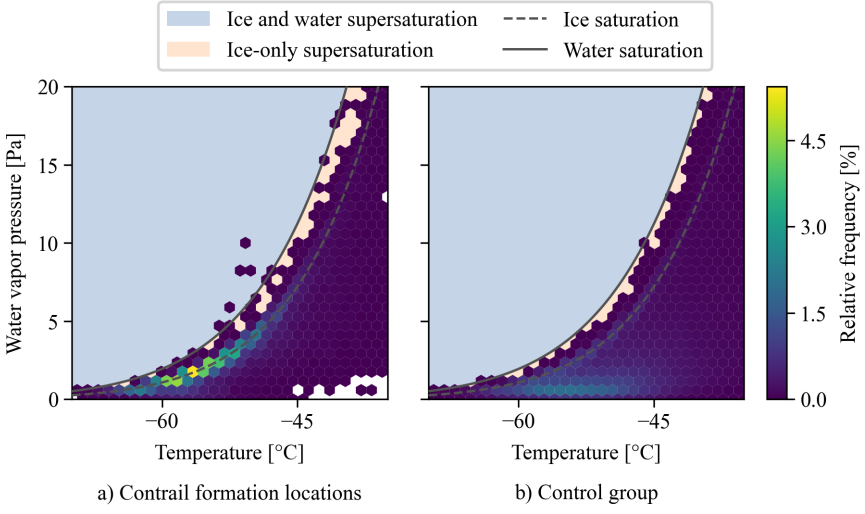

Figure 15. Joint distributions of temperature and water vapor partial pressure at inferred contrail formation locations (left) and across the reference flight population (right). The ice and liquid-water saturation curves delineate the corresponding supersaturation regimes.

Figure 16 shows the same data again, this time in an altitude–temperature diagram together with the contrail formation region predicted by the Schmidt–Appleman criterion for an engine efficiency of 0.3. The ISA standard atmosphere is also shown. Altitude is calculated from pressure using the standard barometric relation of the International Standard Atmosphere (ISA). Again, the contrail formation locations are concentrated at temperatures between -60 and -50 °C and at altitudes between

https://doi.org/10.5194/egusphere-2026-6619
Preprint. Discussion started: 23 November 2026
© Author(s) 2026. CC BY 4.0 License.

9 and 12 km in the region of diagram where contrail formation is possible regardless of relative humidity (green). However, contrails were also detected in the red area, where the SAC deems contrail formation impossible.

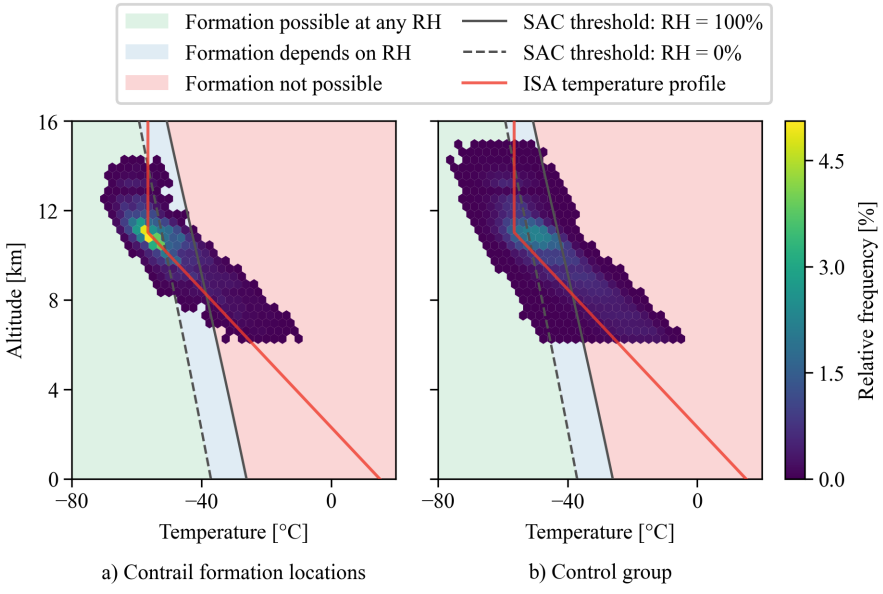

Figure 16. Joint distributions of temperature and pressure altitude at inferred contrail formation locations (left) and across the reference flight population (right). Contrail formation regimes according to the SAC are shown for an assumed constant overall propulsion efficiency, together with the International Standard Atmosphere temperature profile.

4 Discussion

Overall, the proposed method performed well, as a large proportion of the detected contrails could be assigned to corresponding flights, mostly with a good agreement between the observed contrail and the associated flight trajectory. In most cases, the assignments were also relatively unambiguous. Furthermore, the identified environmental conditions were generally consistent with the Schmidt-Appleman criterion, indicating that the resulting contrail-flight matches are plausible. Nevertheless, several sources of uncertainty and potential error remain.

This section discusses these limitations and their possible causes. Particular attention is given to the limited temporal persistence of some detected contrails, unsuccessful contrail-flight assignments, and deviations of the identified environmental conditions from the Schmidt-Appleman criterion.

4.1 Temporal Persistence of Detected Contrails

Around 35% of the detected contrails are identified in only a single time step. There are several possible reasons for this. First, some contrails may in fact persist only for a short period of time. Another observed reason is faulty line segmentation.

https://doi.org/10.5194/egusphere-2026-6619
Preprint. Discussion started: 23 November 2026
© Author(s) 2026. CC BY 4.0 License.

As shown in Figure 4, not every detected line necessarily represents a contrail. Consequently, a certain fraction of the lines produced by the segmentation may not correspond to actual contrails. Such lines may appear only in a single time step, and no corresponding successor can therefore be identified.

4.2 Unmatched Contrails

For approximately 18% of the detected contrails, no corresponding flight could be identified. There are several possible reasons for this. The responsible aircraft may not be included in the available ADS-B data (such as military flights), or the detected contrail may in fact be a false detection caused by the contrail detection algorithm or the line segmentation. Another possibility is an error in the tracking process. In this case, the first identified observation may not correspond to the actual initial observation of the contrail, but to a later stage of its development. As a result, the responsible flight may fall outside the considered time window from $t_0 - 70$ min to t_0. Inaccurate wind data or overly restrictive matching tolerances may also prevent a valid flight from being identified.

4.3 Ambiguity of Contrail-Flight Matching

There are several possible reasons for ambiguous contrail-flight matches. One reason is that a contrail observed in a satellite image may actually consist of two contrails that overlap spatially and therefore appear as a single contrail from above.

Another reason is that multiple flights may follow very similar routes with typical operational separation that may fall below the frequency of the satellite imagery. Furthermore, these flights then experience similar wind conditions. In such cases, the accuracy of the method may not be sufficient to distinguish between the corresponding hypothetical contrail trajectories. This limitation is mainly caused by the spatial resolution of the satellite imagery and the quality of the wind data. It may be reduced by using higher-quality source data or by adjusting the detection thresholds more appropriately.

4.4 Inconsistencies with the Schmidt–Appleman Criterion

The inconsistencies with the Schmidt-Appleman criterion described in Section 3.3 may have two main causes: incorrect contrail-flight matching or inaccuracies in the atmospheric data. To distinguish between these effects, a high-confidence subset of the contrail formation locations was created. This subset includes only matches with a quality score above 0.4, a confidence score above 0.7, and at least three tracked time steps.

Figure 17 compares the temperature and relative humidity distributions of this high-confidence subset with those of the complete set of identified contrail formation locations. For temperature, almost no data points above -30 °C remain in the high-confidence subset. This indicates that the previously observed formation conditions at comparatively high temperatures are most likely caused by incorrect matches produced by the proposed method.

For relative humidity, the high-confidence subset considerably reduces the number of data points below approximately 50% relative humidity. However, the large fraction of data below 100% relative humidity remains largely unchanged. This suggests that these deviations may not primarily result from incorrect matching, but instead from limitations of the underlying

https://doi.org/10.5194/egusphere-2026-6619
Preprint. Discussion started: 23 November 2026
© Author(s) 2026. CC BY 4.0 License.

atmospheric data. The atmospheric dataset has a spatial resolution of approximately 31 km and a temporal resolution of one hour. Due to the strong spatial and temporal variability of relative humidity, interpolation between these grid points may therefore not reproduce the actual local humidity conditions with sufficient accuracy.

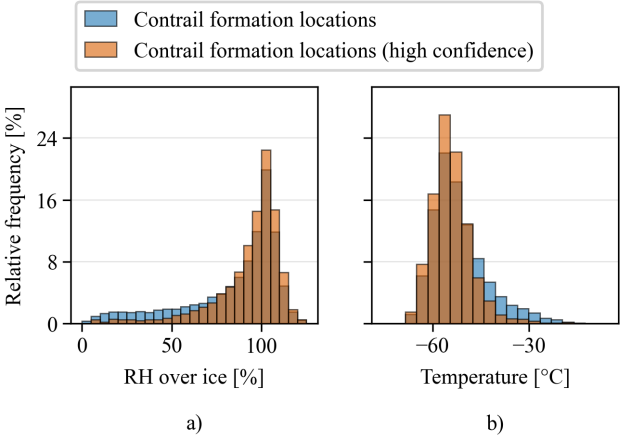

Figure 17. Comparison of the temperature and relative humidity distributions for all identified contrail formation locations and the high-confidence subset. The high-confidence subset includes only matches with a quality score above 0.4, a confidence score above 0.7, and at least three tracked time steps.

5 Conclusions

An optimized and refined approach for an observation-based characterization of the conditions at contrail formation was presented. Based on this approach, the relevant parameters that characterize the contrail formation were investigated and compared to theoretical models. First, the geographical positions of contrails were determined using a public machine learning-based contrail detection model. Subsequently, the detected contrail segments were grouped temporally and spatially using a newly developed line segmentation and tracking algorithm. This made it possible to identify both the location and time of the first observation of a given contrail, as well as the temporal progression of the contrails. This information was then used to identify the originating flight using an optimized and adapted tracking algorithm, and to determine the point of origin of the contrail along its trajectory.

The approach was applied to observation data of 53 Mondays in 2025, each 24 hours long, across a 1100 km wide and high area in North America. In doing so, the environmental conditions were determined for over 25,000 flight-contrail pairs. It was shown that the determined environmental conditions generally correspond to the behaviour predicted by the Schmidt–Appleman criterion. However, in many cases the actual relative humidity encountered in the atmospheric data is lower than would be expected for the formation of persistent contrails. This could be due to uncertainties in the atmospheric data used and therefore does not necessarily indicate a weakness in the method developed. By comparing the environmental conditions at the time of contrail

https://doi.org/10.5194/egusphere-2026-6619
Preprint. Discussion started: 23 November 2026
© Author(s) 2026. CC BY 4.0 License.

formation with the results of the previous method, it was demonstrated that the optimizations implemented here lead to a significantly improved classification quality. However, given the small theoretical influence, this is in line with expectations. The results of this study highlight several possibilities for the further development and application of the approach. First, further validation of the approach would be useful, for example through comparison with manual or automated ground-based observations of contrails. Furthermore, applying the approach to additional temporal and geographical extent would be of interest in order to investigate possible regional or seasonal differences. In addition, a comparison with existing contrail modelling and prediction models would be relevant.

Outlook

The conditions under which contrails form depend not only on environmental conditions but also on the engine operating conditions and its emissions. For this purpose and to complete the picture shown in fig. 1, a thermodynamic cycle model is necessary. Given the now readily available conditions at the contrail origin and the aircraft performance data derived from the flight trajectory, the boundary conditions for an engine model are available along with the crucial information whether a contrail has actually occurred or not. Along with a combustion chamber model, this approach can then provide an enriched dataset for future use.

By applying this approach initially to the in-house V2500 research engine and thereby single-aisle aircraft of the Airbus A320 family, over 5000 flights remain from within the analyzed dataset. For the research engine, validated tools such as the in-house performance model (Goeing et al., 2024) and combustion chamber models (**??**) are available to provide additional information such as soot particle emissions. This opens up a huge amount of data for further processing with correlation-based or machine learning tools, which might be able to detect additional pattern regarding contrail formation.

Video supplement. Examples for tracking of real data: https://leopard.tu-braunschweig.de/receive/dbbs$_{m}ods_{0}$0080271

Author contributions. Conceptualization, S.L,J.G.; methodology, S.K,S.L; software, S.K; validation, S.K., S.L.; formal analysis, S.K.; investigation, S.K.; resources, J.G.; data curation, S.K.; writing—original draft preparation, S.K., S.L.; writing—review and editing, S.K., S.L., J.G.; visualization, S.K., S.L.; supervision, S.L., J.G.; project administration, S.L.,J.G.; funding acquisition, J.G.; All authors have read and agreed to the published version of the manuscript.

Competing interests. The authors declare no conflicts of interest. This research received no external funding.

https://doi.org/10.5194/egusphere-2026-6619
Preprint. Discussion started: 23 November 2026
© Author(s) 2026. CC BY 4.0 License.

References

Bickel, M., Ponater, M., Burkhardt, U., Righi, M., Hendricks, J., and Jöckel, P.: Contrail Cirrus Climate Impact: From Radiative Forcing to Surface Temperature Change, Journal of Climate, 38, 1895–1912, https://doi.org/10.1175/JCLI-D-24-0245.1, 2025.

Chevallier, R., Shapiro, M., Engberg, Z., Soler, M., and Delahaye, D.: Linear Contrails Detection, Tracking and Matching with Aircraft Using Geostationary Satellite and Air Traffic Data, Aerospace, 10, 578, https://doi.org/10.3390/aerospace10070578, 2023.

Crouse, D. F.: On implementing 2D rectangular assignment algorithms, IEEE Transactions on Aerospace and Electronic Systems, 52, 1679–1696, https://doi.org/10.1109/TAES.2016.140952, 2016.

Debnath, S.: Line-Segment-Detector-using-OpenCV, 2020.

Goeing, J., Lück, S., and Friedrichs, J.: A Validated Unsteady Turbofan Engine Performance Simulation Using Pseudo Bond Graph Approach, in: Volume 1: Aircraft Engine, p. V001T01A014, American Society of Mechanical Engineers, London, United Kingdom, ISBN 978-0-7918-8792-9, https://doi.org/10.1115/GT2024-122738, 2024.

Hersbach, H., Bell, B., Berrisford, P., Hirahara, S., Horányi, A., Muñoz-Sabater, J., Nicolas, J., Peubey, C., Radu, R., Schepers, D., Simmons, A., Soci, C., Abdalla, S., Abellan, X., Balsamo, G., Bechtold, P., Biavati, G., Bidlot, J., Bonavita, M., De Chiara, G., Dahlgren, P., Dee, D., Diamantakis, M., Dragani, R., Flemming, J., Forbes, R., Fuentes, M., Geer, A., Haimberger, L., Healy, S., Hogan, R. J., Hólm, E., Janisková, M., Keeley, S., Laloyaux, P., Lopez, P., Lupu, C., Radnoti, G., de Rosnay, P., Rozum, I., Vamborg, F., Villaume, S., and Thépaut, J.: The ERA5 global reanalysis, Quarterly Journal of the Royal Meteorological Society, 146, 1999–2049, https://doi.org/10.1002/qj.3803, 2020.

Jeßberger, P., Voigt, C., Schumann, U., Sölch, I., Schlager, H., Kaufmann, S., Petzold, A., and Schäuble, D.: Aircraft type influence on contrail properties, Atmos. Chem. Phys., 2013.

Kode, J.: Google Research Identify Contrails Reduce Global Warming Jun Koda 1st Place Solution, https://www.kaggle.com/competitions/google-research-identify-contrails-reduce-global-warming/writeups/jun-koda-1st-place-solution, available online at: https://www.kaggle.com/competitions /google-research-identify-contrails-reduce-global-warming /writeups/jun-koda-1st-place-solution, last accessed on 1. Jan. 2026., 2023.

Kröger, S., Lück, S., and Goeing, J.: AI- and Data-driven Identification of Contrail Sources, p. 12 pages, https://doi.org/10.25967/650223, artwork Size: 12 pages Medium: application/pdf Version Number: 1.0, 2025.

Kuhn, H. W.: The Hungarian Method for the Assignment Problem, in: 50 Years of Integer Programming 1958-2008, edited by Jünger, M., Liebling, T. M., Naddef, D., Nemhauser, G. L., Pulleyblank, W. R., Reinelt, G., Rinaldi, G., and Wolsey, L. A., pp. 29–47, Springer Berlin Heidelberg, Berlin, Heidelberg, ISBN 978-3-540-68274-5 978-3-540-68279-0, https://doi.org/10.1007/978-3-540-68279-0_2, 2010.

Kärcher, B.: Formation and radiative forcing of contrail cirrus, Nature Communications, 9, 1824, https://doi.org/10.1038/s41467-018-04068-0, 2018.

Lee, D., Fahey, D., Skowron, A., Allen, M., Burkhardt, U., Chen, Q., Doherty, S., Freeman, S., Forster, P., Fuglestvedt, J., Gettelman, A., De León, R., Lim, L., Lund, M., Millar, R., Owen, B., Penner, J., Pitari, G., Prather, M., Sausen, R., and Wilcox, L.: The contribution of global aviation to anthropogenic climate forcing for 2000 to 2018, Atmospheric Environment, 244, 117 834, https://doi.org/10.1016/j.atmosenv.2020.117834, 2021.

Lieder, D., Bień, M., Seume, E., Lück, S., Ferraro, F., Friedrichs, J., and Goeing, J.: Performance and Emission Analysis of Aircraft Engines Under Realistic Conditions, International Journal of Turbomachinery, Propulsion and Power, 11, 2, https://doi.org/10.3390/ijtpp11010002, 2025.

https://doi.org/10.5194/egusphere-2026-6619
Preprint. Discussion started: 23 November 2026
© Author(s) 2026. CC BY 4.0 License.



Matas, J., Galambos, C., and Kittler, J.: Robust Detection of Lines Using the Progressive Probabilistic Hough Transform, Computer Vision and Image Understanding, 78, 119–137, https://doi.org/10.1006/cviu.1999.0831, 2000.

Meijer, V. R., Eastham, S. D., Waitz, I. A., and Barrett, S. R. H.: Contrail altitude estimation using GOES-16 ABI data and deep learning, Atmospheric Measurement Techniques, 17, 6145–6162, https://doi.org/10.5194/amt-17-6145-2024, 2024.

Ng, J. Y.-H., McCloskey, K., Cui, J., Meijer, V. R., Brand, E., Sarna, A., Goyal, N., Van Arsdale, C., and Geraedts, S.: OpenContrails: Benchmarking Contrail Detection on GOES-16 ABI, https://doi.org/10.48550/ARXIV.2304.02122, version Number: 2, 2023.

Ng, J. Y.-H., McCloskey, K., Cui, J., Meijer, V. R., Brand, E., Sarna, A., Goyal, N., Van Arsdale, C., and Geraedts, S.: Contrail Detection on GOES-16 ABI With the OpenContrails Dataset, IEEE Transactions on Geoscience and Remote Sensing, 62, 1–14, https://doi.org/10.1109/TGRS.2023.3345226, 2024.

Olive, X.: traffic, a toolbox for processing and analysing air traffic data, Journal of Open Source Software, 4, 1518, https://doi.org/10.21105/joss.01518, 2019.

Olive, X., Krummer, J., Figuet, B., and Alligier, R.: Filtering Techniques for ADS-B Trajectory Preprocessing, Journal of Open Aviation Science, 2, https://doi.org/10.59490/joas.2024.7882, 2025.

Riggi-Carrolo, E., Dubot, T., Sarrat, C., and Bedouet, J.: AI-Driven Identification of Contrail Sources: Integrating Satellite Observation and Air Traffic Data, Journal of Open Aviation Science, 1, https://doi.org/10.59490/joas.2023.7209, 2023.

Roosenbrand, E., Sun, J., and Hoekstra, J.: Contrail minimization through altitude diversions: A feasibility study leveraging global data, Transportation Research Interdisciplinary Perspectives, 22, 100 953, https://doi.org/10.1016/j.trip.2023.100953, 2023.

Sarna, A., Meijer, V., Chevallier, R., Duncan, A., McConnaughay, K., Geraedts, S., and McCloskey, K.: Benchmarking and improving algorithms for attributing satellite-observed contrails to flights, https://doi.org/10.5194/egusphere-2024-3664, 2025.

Sausen, R., Hofer, S., Gierens, K., Bugliaro, L., Ehrmanntraut, R., Sitova, I., Walczak, K., Burridge-Diesing, A., Bowman, M., and Miller, N.: Can we successfully avoid persistent contrails by small altitude adjustments of flights in the real world?, Meteorologische Zeitschrift, 33, 83–98, https://doi.org/10.1127/metz/2023/1157, 2024.

Schafer, M., Strohmeier, M., Lenders, V., Martinovic, I., and Wilhelm, M.: Bringing up OpenSky: A large-scale ADS-B sensor network for research, in: IPSN-14 Proceedings of the 13th International Symposium on Information Processing in Sensor Networks, pp. 83–94, IEEE, Berlin, Germany, ISBN 978-1-4799-3147-7 978-1-4799-3146-0, https://doi.org/10.1109/IPSN.2014.6846743, 2014.

Schumann, U.: On conditions for contrail formation from aircraft exhausts, 1996.

Schumann, U.: A contrail cirrus prediction model, Geoscientific Model Development, 5, 543–580, https://doi.org/10.5194/gmd-5-543-2012, 2012.

Schumann, U. and Heymsfield, A. J.: On the Life Cycle of Individual Contrails and Contrail Cirrus, Meteorological Monographs, 58, 3.1–3.24, https://doi.org/10.1175/AMSMONOGRAPHS-D-16-0005.1, 2017.

Schumann, U., Baumann, R., Baumgardner, D., Bedka, S. T., Duda, D. P., Freudenthaler, V., Gayet, J.-F., Heymsfield, A. J., Minnis, P., Quante, M., Raschke, E., Schlager, H., Vázquez-Navarro, M., Voigt, C., and Wang, Z.: Properties of individual contrails: a compilation of observations and some comparisons, Atmospheric Chemistry and Physics, 17, 403–438, https://doi.org/10.5194/acp-17-403-2017, 2017.

Sun, J., Olive, X., Roosenbrand, E., Parzani, C., and Strohmeier, M.: OpenSky Report 2024: Analysis of Global Flight Contrail Formation and Mitigation Potential, in: 2024 AIAA DATC/IEEE 43rd Digital Avionics Systems Conference (DASC), pp. 1–10, IEEE, San Diego, CA, USA, ISBN 979-8-3503-4961-0, https://doi.org/10.1109/DASC62030.2024.10748832, 2024.

Teoh, R., Schumann, U., Majumdar, A., and Stettler, M. E. J.: Mitigating the Climate Forcing of Aircraft Contrails by Small-Scale Diversions and Technology Adoption, Environmental Science & Technology, 54, 2941–2950, https://doi.org/10.1021/acs.est.9b05608, 2020.

https://doi.org/10.5194/egusphere-2026-6619
Preprint. Discussion started: 23 November 2026
© Author(s) 2026. CC BY 4.0 License.



Teoh, R., Engberg, Z., Schumann, U., Voigt, C., Shapiro, M., Rohs, S., and Stettler, M.: Global aviation contrail climate effects from 2019 to 2021, https://doi.org/10.5194/egusphere-2023-1859, 2023.

535 Vazquez-Navarro, M., Mannstein, H., and Mayer, B.: An automatic contrail tracking algorithm, Atmospheric Measurement Techniques, 3, 1089–1101, https://doi.org/10.5194/amt-3-1089-2010, 2010.

Xiaolong, Y.: Skeleton Network, available online at: https://github.com/Image-Py/sknw, last accessed on 31. Jan 2025., 2021.